Enhancing the Performance of the Half Tin and Half Lead Perovskite Solar Cells by Suppression of the Bulk and Interfacial Charge Recombination

Shao, Shuyan; Cui, Yong; Duim, Herman; Qiu, Xinkai; Dong, Jingjin; ten Brink, Gert H.; Portale, Giuseppe; Chiechi, Ryan C.; Zhang, Shaoqing; Hou, Jianhui

Published in:
Advanced materials

DOI:
10.1002/adma.201803703

Publication date:
2018

Enhancing the Performance of the Half Tin and Half Lead Perovskite Solar Cells by Suppression of the Bulk and Interfacial Charge Recombination

Shuyan Shao, Yong Cui, Herman Duim, Xinkai Qiu, Jingjin Dong, Gert H. ten Brink, Giuseppe Portale, Ryan C. Chiechi, Shaoqing Zhang, Jianhui Hou, and Maria Antonietta Loi**

In this article it is investigated how the hole extraction layer (HEL) influence the charge recombination and performance in half tin and half lead ($FASn_{0.5}Pb_{0.5}I_3$) based solar cells (HPSCs). $FASn_{0.5}Pb_{0.5}I_3$ film grown on PEDOT:PSS displays a large number of pin-holes and open grain boundaries, resulting in a high defect density and shunts in the perovskite film causing significant bulk and interfacial charge recombination in the HPSCs. By contrast, $FASn_{0.5}Pb_{0.5}I_3$ films grown on PCP-Na, an anionic conjugated polymer, show compact and pin-hole free morphology over a large area, which effectively eliminates the shunts and trap states. Moreover, PCP-Na is characterized by a higher work function, which determines a favorable energy alignment at the anode interface, enhancing the charge extraction. Consequently, both the interfacial and bulk charge recombination in devices using PCP-Na HEL are considerably reduced giving rise to an overall improvement of all the device parameters. The HPSCs fabricated with this HEL display power conversion efficiency up to 16.27%, which is 40% higher than the efficiency of the control devices using PEDOT:PSS HEL (11.60%). Furthermore, PCP-Na as HEL offers superior performance in larger area devices compared to PEDOT:PSS.

Organic metal halide perovskites are regarded as ideal light absorbing materials for photovoltaic devices since they possess high absorption coefficient, high charge carrier mobility, balanced charge transport, and long charge carrier diffusion length. So far, lead halide perovskites have been studied mostly in single junction solar cells, and only after about eight years of optimization of the film morphology and device structure they achieved record power conversion efficiency (PCE) approaching 23.0%.[1–14]

However, the toxicity of lead causes big concerns about their large-scale application. This motivated the research toward efficient lead-free hybrid perovskite solar cells (HPSCs). Tin, which displays a similar electron configuration of lead, is regarded as a promising alternative. Hybrid perovskites based on Sn have excellent optical absorption and charge carrier transport, but tin-based HPSCs are still suffering from low PCE due to the intrinsic tin vacancies and oxidation of the Sn^{2+}.[15–17] However, recently we have demonstrated that this spontaneous doping can be reduced using traces of 2D tin perovskite, which induces a preferential crystallization of the 3D tin perovskite, and results in a record PCE of 9%.[17]

Dr. S. Shao, H. Duim, Prof. M. A. Loi
Photophysics and OptoElectronics
Zernike Institute for Advanced Materials
University of Groningen
Nijenborgh 4, 9747 AG Groningen, The Netherlands
E-mail: m.a.loi@rug.nl

Y. Cui, Dr. S. Zhang, Prof. J. Hou
State Key Laboratory of Polymer Physics and Chemistry
Beijing National Laboratory for Molecular Sciences
Institute of Chemistry
Chinese Academy of Sciences
Beijing 100190, China
E-mail: hjhzlz@iccas.ac.cn

The ORCID identification number(s) for the author(s) of this article can be found under https://doi.org/10.1002/adma.201803703.

DOI: 10.1002/adma.201803703

X. Qiu, Prof. R. C. Chiechi
Zernike Institute for Advanced Materials
University of Groningen
Nijenborgh 4, 9747 AG Groningen, The Netherlands

X. Qiu, Prof. R. C. Chiechi
Stratingh Institute for Chemistry
University of Groningen
Nijenborgh 4, 9747 AG Groningen, The Netherlands

J. Dong, Dr. G. Portale
Macromolecular Chemistry and New Polymeric Material
Zernike Institute for Advanced Materials
University of Groningen
Nijenborgh 4, 9747 AG Groningen, The Netherlands

G. H. ten Brink
Nanostructured Materials and Interfaces
Zernike Institute for Advanced Materials
University of Groningen
Nijenborgh 4, 9747 AG Groningen, The Netherlands

Recent studies showed that replacing lead by tin in hybrid perovskites, results in an anomalous bandgap behavior, with its reduction from 1.5 to about 1.2 eV with Sn/Pb ratio varied from 0 to 1. The reduction of the bandgap results in the extension of the absorption spectrum further into the near-infrared region.[18,19] Interestingly, the presence of Pb^{2+} appears to be able to stabilize Sn^{2+} in the perovskite structure, reducing the p-doping concentration of the corresponding film compared to pure Sn perovskite films. Moreover, the mixed tin and lead perovskites with bandgap between 1.2 and 1.3 eV are among the ideal candidates as light absorbers for the narrow bandgap subcell in a tandem device based only on perovskites.[20]

These intriguing properties of the mixed tin and lead perovskite materials have motivated intensive research in the last few years. In 2014, Ogomi et al. reported the first HPSCs using mixed tin and lead $MASn_xPb_{(1-x)}I_3$ ($MA = CH_3NH_3$) where x was varied from 0 to 1, as light absorbing layer in a conventional device structure with compact TiO_2 as electron extraction layer (EEL), mesoporous TiO_2 as scaffold and P3HT as hole extraction layer (HEL).[18] These authors obtained a PCE of 4.18% in half lead and half tin ($MASn_{0.5}Pb_{0.5}I_3$) based HPSC. Soon after, Hao et al. reported $MASn_xPb_{(1-x)}I_3$ based HPSCs with the same device configuration but using Spiro-OMeTAD as HEL, displaying a PCE up to 7.37%.[19] This device structure has obvious drawbacks such as the high-temperature processing of the TiO_2 scaffold and the potential damage or oxidation of the Sn perovskite due to the p-dopant (lithium and cobalt salts) used in the HEL. Zuo et al. investigated the composition of $MASn_xPb_{(1-x)}I_3$ film on the device performance of an inverted p–i–n planar device structure, where PEDOT:PSS and PCBM were used as HEL and EEL, respectively. In this configuration they reported a PCE of 10.1% only when the tin content was as low as 15%.[21] After this pioneer work, more papers appeared using the inverted device structure due to its easy and low temperature processing. Yang et al. improved the morphology of the $CH_3NH_3Sn_xPb_{(1-x)}I_3$ film by combining the mixed solvents and antisolvent dripping method, obtaining a PCE of 14.35% for an absorber based on $MASn_{0.25}Pb_{0.75}I_3$.[22] With the motivation to remove more Pb and obtain narrower bandgap perovskite, Lyu et al. worked on $MASn_{0.5}Pb_{0.5}I_3$ films using the chlorobenzene-assisted antisolvent dripping method, obtaining devices with a PCE of 7%.[23] Eperon et al. obtained smooth, highly crystalline and uniform $FASn_{0.5}Pb_{0.5}I_3$ film by using a precursor-phase antisolvent immersion technique, leading to a PCE of 10.9% in a single junction HPSC.[24] Interestingly, substitution of 25% of the FA cations with Cs (cesium) cations significantly improved the PCE of the cell to 14.8%. Zhao et al. demonstrated high quality $FA_{0.6}MA_{0.4}Sn_{0.6}Pb_{0.4}I_3$ film, and achieved a PCE of 17.5% in a single junction cell.[25] Despite the encouraging progress, the PCE of the mixed tin and lead based single junction HPSC is still lower than the Pb-based solar cells.

To summarize, in the past four years the research efforts on mixed tin and lead HPSCs were almost exclusively devoted to tuning the composition and the deposition method of the perovskite film, whereas very little work has been done to improve the device structure and the interface with the perovskite active layer, which are very critical in determining the device performance. To date, PEDOT:PSS has been the most frequently used HEL in mixed tin and lead HPSCs in the inverted planar device structure. However, its strong acidity causes the degradation of the anode interface.[26] Moreover, its work function (about −5.1 eV) does not perfectly match the low-lying valence band (VB) of the half tin and half lead perovskite, reducing the open-circuit voltage (V_{OC}) and short-circuit current density (J_{SC}).[27–30]

Herein, we investigate how the hole transport materials and its interface with the perovskite active layer influences the device performance in the p–i–n half tin and half lead ($FASn_{0.5}Pb_{0.5}I_3$) HPSCs. For the first time, we employed a pH neutral anionic conjugated polymer with alkylsulfonate side group, PCP-Na, as HEL in mixed tin and lead HPSC. The devices using this new HEL show a V_{OC} of 0.78 V, a J_{SC} of 28.51 mA cm^{-2}, a fill factor (FF) of 0.73, and a PCE of 16.27%, which are substantially higher than the values obtained with the control devices using PEDOT:PSS (V_{OC} of 0.61 V, a J_{SC} of 27.80 mA cm^{-2}, an FF of 0.68, and PCE of 11.60%). The considerable improvement in the device performance is attributed to the unique properties of PCP-Na. Compared to PEDOT:PSS, PCP-Na possesses higher work function (−5.2 eV), which allows a better energy alignment with the valence band of the perovskite layer, enhancing built-in potential and charge extraction efficiency. Moreover, PCP-Na induces the growth of uniform, compact and pin-hole free $FASn_{0.5}Pb_{0.5}I_3$ film over large area, reducing the interfacial and bulk charge recombination significantly. Interestingly, PCP-Na offers superior performance in large area HPSCs due to combined advantages of its high conductivity and formation of the uniform large area $FASn_{0.5}Pb_{0.5}I_3$ film compared to PEDOT:PSS.

In HPSCs the extraction and recombination of the charge carriers highly depend on the energy alignment and the trap states at perovskite/charge transport layer interfaces as well as charge transport in the charge transport materials.[5,9,27] Moreover, the bottom charge transport layer also has great influence on the morphology of the perovskite film, which in turn affects the trap states at the interfaces and in the bulk of the perovskite film and therefore the charge recombination in the device.

Figure 1a shows the chemical structure of PCP-Na, which was synthesized by Cui et al.[26] Figure 1b shows the energy levels as are reported in literature for the various layers in the planar device structure used in this work, where PCP-Na or PEDOT:PSS are used as HEL, $FASn_{0.5}Pb_{0.5}I_3$ is the light absorbing layer, C_{60} is the electron transport layer and bathocuproine (BCP) is employed as a hole blocking layer.[17,26] Compared to PEDOT:PSS, the work function of PCP-Na matches better with the VB (−5.6 eV) of the $FASn_{0.5}Pb_{0.5}I_3$ film, which not only facilitates the hole extraction at the $FASn_{0.5}Pb_{0.5}I_{3/}$PCP-Na interface, but also enlarges the built-in potential in the device.

Cui et al. reported that PCP-Na has a high electrical conductivity of 1.66×10^{-3} S cm^{-1} slightly higher than PEDOT:PSS (1.35×10^{-3} S cm^{-1}), due to the self-doping of the polymer by the delocalized radical electrons.[26] We investigated the surface morphologies of the indium tin oxide (ITO) electrodes modified with PEDOT:PSS and PCP-Na by atomic force microscopy (AFM), as shown in Figure 1c,d. Similar to PEDOT:PSS, PCP-Na forms very compact, homogenous and smooth film with surface roughness of 4 nm on top of the ITO substrate, which enables a uniform interfacial contact with the perovskite

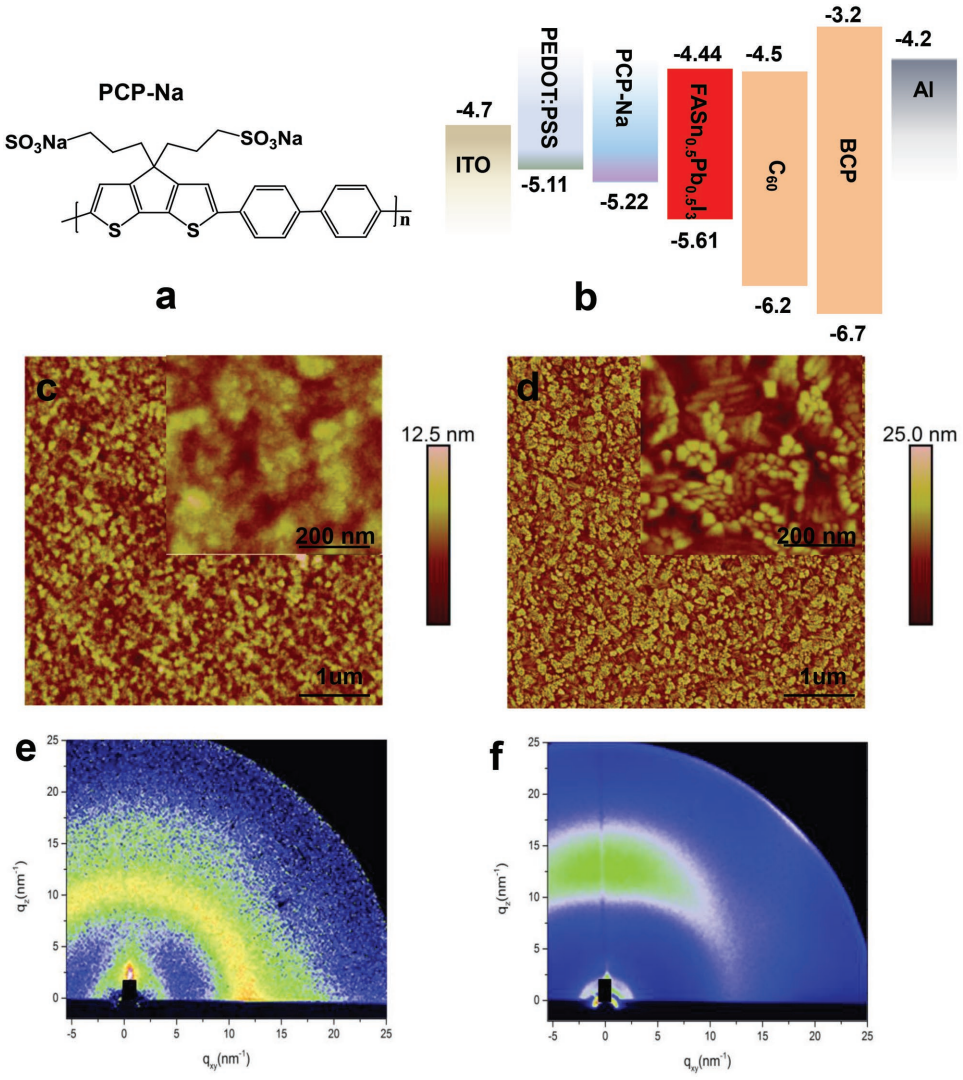

Figure 1. a) Schematic of the chemical structure of PCP-Na. b) Diagram of the energy levels of the various layers used in the device structure. AFM topographical images of c) PEDOT:PSS, d) PCP-Na. GIWAXS images of e) PEDOT:PSS and f) PCP-Na thin films.

layer, and also reduces the possibility to form shunts. The device performance is independent on the thickness of PCP-Na when this is varied from 1.5 to 10 nm as shown in Figure S1 of the Supporting Information, which is attributed to the good film forming properties of the conjugated polyelectrolyte and its high conductivity. Unlike PEDOT:PSS, which displays isotropic morphology, PCP-Na forms patterns due to its crystallization. Grazing incidence wide-angle X-ray scattering (GIWAXS) measurements in Figure 1e reveals the amorphous nature of PEDOT:PSS, while PCP-Na displays (Figure 1f) higher crystallinity with its backbone lying parallel to the substrate (face-on orientation), which is favorable for charge extraction in the solar cells. Compared to the device using PEDOT:PSS, the device using PCP-Na as HEL shows considerable improvement in all the parameters including V_{OC}, J_{SC}, FF, and PCE, as it is displayed by the *J*–*V* characteristics of the fully optimized devices in **Figure 2**a. Furthermore, the control device using PEDOT:PSS HEL display an obvious hysteresis in the *J*–*V* curves. In the forward sweep, the device shows a V_{OC} of 0.61 V, a J_{SC} of 27.80 mA cm^{-2}, an FF of 0.68, and a PCE 11.60% (**Table 1**). In the reverse sweep, the device has a V_{OC} of 0.58 V, a J_{SC} of 26.54 mA cm^{-2}, an FF of 0.61, and a PCE of 9.46%.

At the opposite, device using PCP-Na HEL displays a negligible hysteresis in the *J*–*V* curves. Their forward sweep shows a V_{OC} of 0.77 V, a J_{SC} of 29.30 mA cm^{-2}, an FF of 0.71, and a PCE of 15.96%. While the reverse sweep, displays a V_{OC} of 0.78 V, a J_{SC} of 28.51 mA cm^{-2}, an FF of 0.73, and a PCE of 16.27%. This is a 40% improvement of the PCE compared to devices using PEDOT:PSS as HEL.

Figure 2b shows the *J*–*V* curves for devices using PCP-Na HEL measured at different sweep rates, which shows very small hysteresis and characteristics independent of the sweep rate. The steady state PCE tracked at maximum power point for the devices using PCP-Na HEL is measured to be 15.50% (see Figure S2, Supporting Information).

Figure 2c shows the conversion efficiency of the incident photons to electrons (IPCE) for the two types of devices, confirming the improvement in the photocurrent density of the

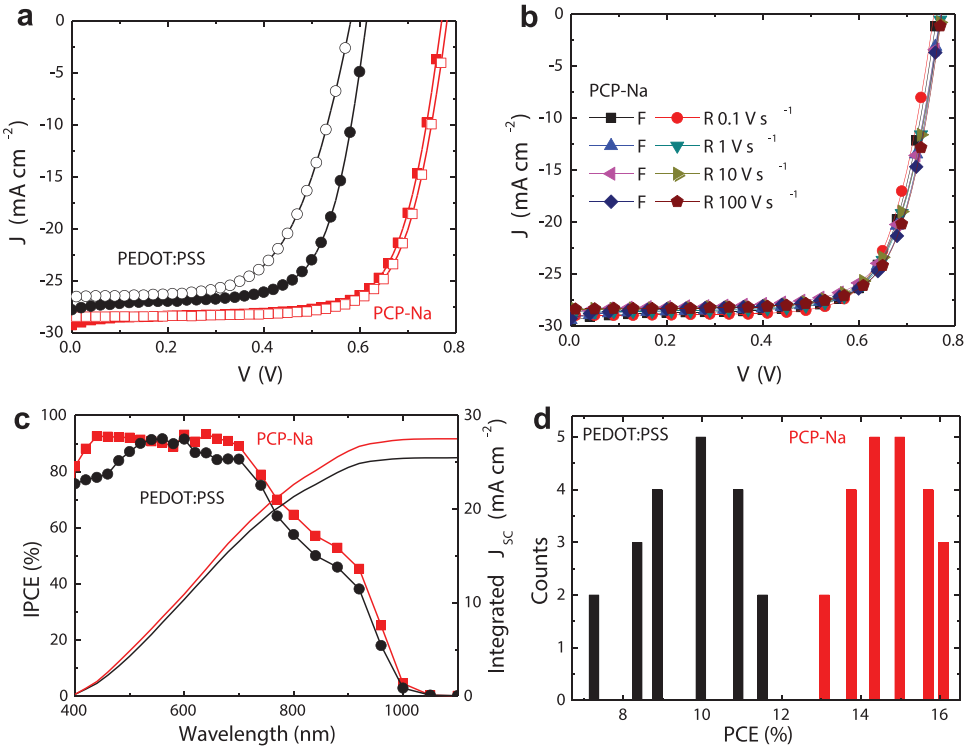

Figure 2. a) *J–V* curves of the champion devices using PEDOT:PSS and PCP-Na HELs under 1 sun illumination (the empty and solid symbols represent reverse and forward sweep, respectively). b) *J–V* curves of the champion device fabricated with PCP-Na as HEL tested with different sweep rates. c) IPCE spectra for the two types of devices. d) Statistics of power conversion efficiency for devices using PEDOT:PSS and PCP-Na as HEL.

device using PCP-Na as HEL. The current density integrated from the IPCE data is 25.72 and 27.70 mA cm^{-2} for the two devices using PEDOT:PSS and PCP-NA, respectively, which show a very small deviation (<10%) respect to the values obtained from the *J–V* curves.

We fabricated about 20 devices using each HEL to perform basic statistics and understand the robustness of the processing of the two HELs, the histogram summarizing the experiments is reported in Figure 2d. The devices using PCP-Na HEL have much higher reproducibility evidenced by the much narrower distribution of the device performance respect to the ones using PEDOT:PSS. At this point it is important to understand the reason of the better performances of devices using PCP-Na as HEL.

Figure S3a of the Supporting Information reports the transmission spectra of PEDOT:PSS and PCP-Na thin films on quartz substrate. PCP-Na displays a much higher transparency (except for the region between 420 and 530 nm) in most of the solar spectrum range where the $FASn_{0.5}Pb_{0.5}I_3$ active layer absorbs (see Figure S3b, Supporting Information), reducing the photon losses compared to the case of PEDOT:PSS. PCP-Na with higher work function forms more favorable energy alignment with the valence band of the hybrid perovskite, improving the hole extraction. These two factors contribute to the enhancement in the photocurrent density and the IPCE over the spectrum.

Table 1. Performance parameters of the champion devices using PCP-Na and PEDOT:PSS as HEL.

Device	V_{OC} [V]	J_{SC} [mA cm^{-2}]	FF	PCE [%]
PEDOT:PSS	0.610	27.79	0.68	11.60
	0.581	26.54	0.61	9.46
PCP-Na	0.771	29.30	0.71	15.96
	0.782	28.51	0.73	16.27

Figure 3a shows the *J–V* characteristics of the HPSCs using PEDOT:PSS and PCP-Na HELs measured under dark condition. Compared to the device using PEDOT:PSS HEL, the device using PCP-Na has much lower leakage current density. The capacitance versus voltage measurement under dark condition in Figure 3b confirms the improvement of the built-in potential in the device using PCP-Na HEL. The enhanced built-in potential and suppressed shunts in the device using PCP-Na HEL contribute to the large improvement in the V_{OC}.

To further understand the discrepancy in the device performance, we scrutinized the morphology of the $FASn_{0.5}Pb_{0.5}I_3$ films on top of PEDOT:PSS and PCP-Na, respectively. Figure 3c,d shows the scanning electron microscopy (SEM) images of the two samples. The $FASn_{0.5}Pb_{0.5}I_3$ film forms large pin-holes (diameter about 100 nm) on PEDOT:PSS substrate. The SEM image with higher magnification in Figure S4a of the Supporting Information clearly shows that these large pin-holes are locate at grain boundaries and some small pin-holes (diameter ranges from 10 to 30 nm) locate inside the grains. These pin-holes not only cause high leakage current by forming shunts, but also creates high structural defect density around

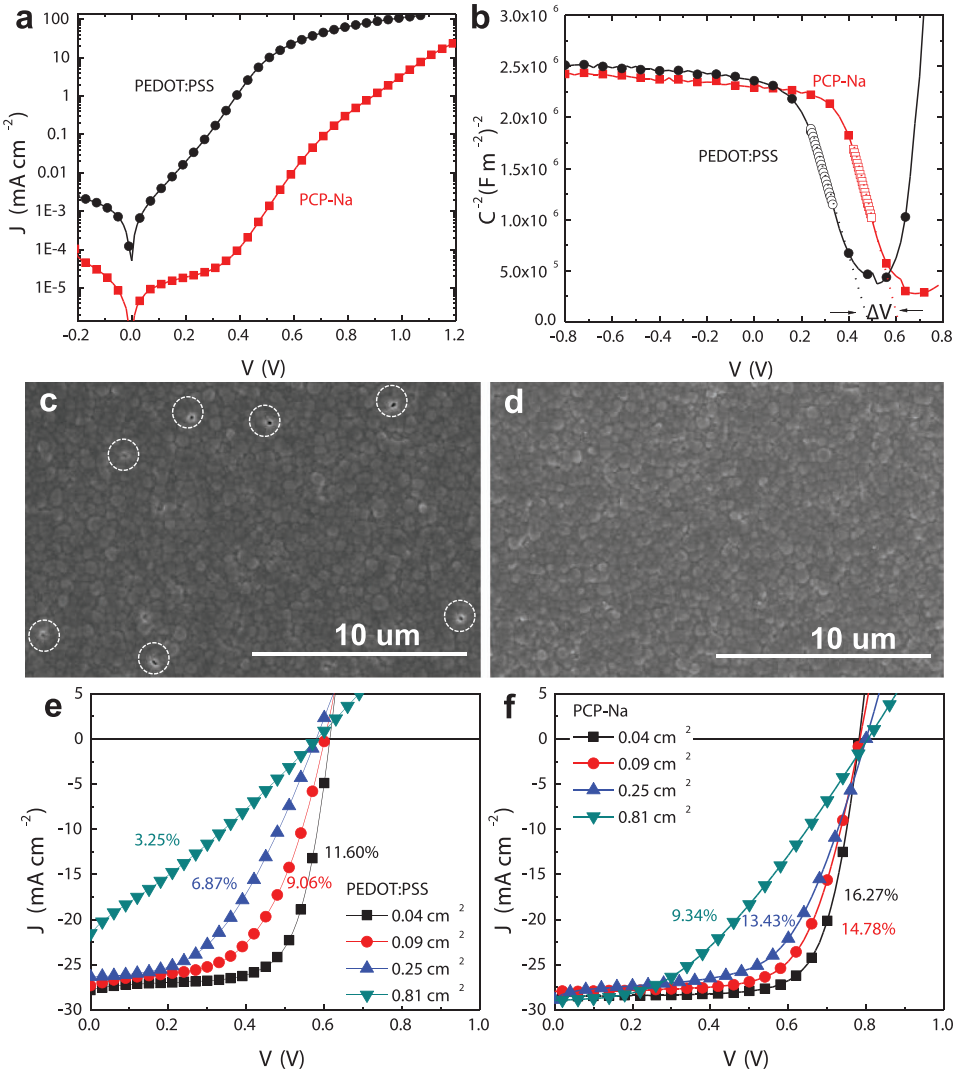

Figure 3. a) *J–V* curves, and b) capacitance versus applied voltage of the devices using PEDOT:PSS and PCP-Na as HELs measured under dark condition (the open symbols represent fitting results in the linear region from Mott–Schottky analysis; ΔV denotes the change in the built-in potential). SEM images of the $FASn_{0.5}Pb_{0.5}I_3$ film on top of c) PEDOT:PSS (the dashed circle denotes the pin-holes), d) PCP-Na. The *J–V* curves under illumination for the device using e) PEDOT:PSS and f) PCP-Na HEL with different device areas.

those "open" grain boundaries and "hollow" grains. Our recent work indicated that the 'open' grain boundaries cause severe trap assisted recombination in HPSCs.[7]

By contrast, uniform, compact and pin-hole free $FASn_{0.5}Pb_{0.5}I_3$ film forms on PCP-Na films (Figure 3b; Figure S4b, Supporting Information), which should help to reduce the number of trap states respect to the film grown on PEDOT:PSS. Furthermore, the grains appear to have fuzzy facets in the $FASn_{0.5}Pb_{0.5}I_3$ film coated on top of PEDOT:PSS (Figure S5a, Supporting Information), while grains grown on top of PCP-Na appear to have more clear facets (Figure S5b, Supporting Information).

Figure S6 of the Supporting Information shows the X-ray diffraction (XRD) patterns for the perovskite films on top of PEDOT:PSS and PCP-Na, which demonstrates single perovskite phase with orthorhombic structure. Moreover, there is no obvious difference in the diffraction peak intensities, which could possibly mean similar intragrains crystallinity in both films.[26]

The formation of uniform, compact and pin-hole free perovskite film is very critical for the fabrication of highly efficient large area device. Figure 3e,f shows the *J–V* curves under illumination of devices of different areas using PEDOT:PSS and PCP-Na as HEL. The device parameters are summarized in Table S1 and Figure S7 of the Supporting Information. The devices using PEDOT:PSS as HEL show decrease in all the performance parameters when the area increases. In particular the device of 0.81 cm^2 area has a PCE of 3.25%, which is a 72% loss compared to the efficiency of devices with 0.04 cm^2 area. The considerable increase in the series resistance (34 Ω cm^2) of the large area device impedes the charge extraction. Moreover, the larger area $FASn_{0.5}Pb_{0.5}I_3$ film on top of PEDOT:PSS has more shunts and more defect states compared to the smaller area one, leading to much higher charge recombination. These two factors

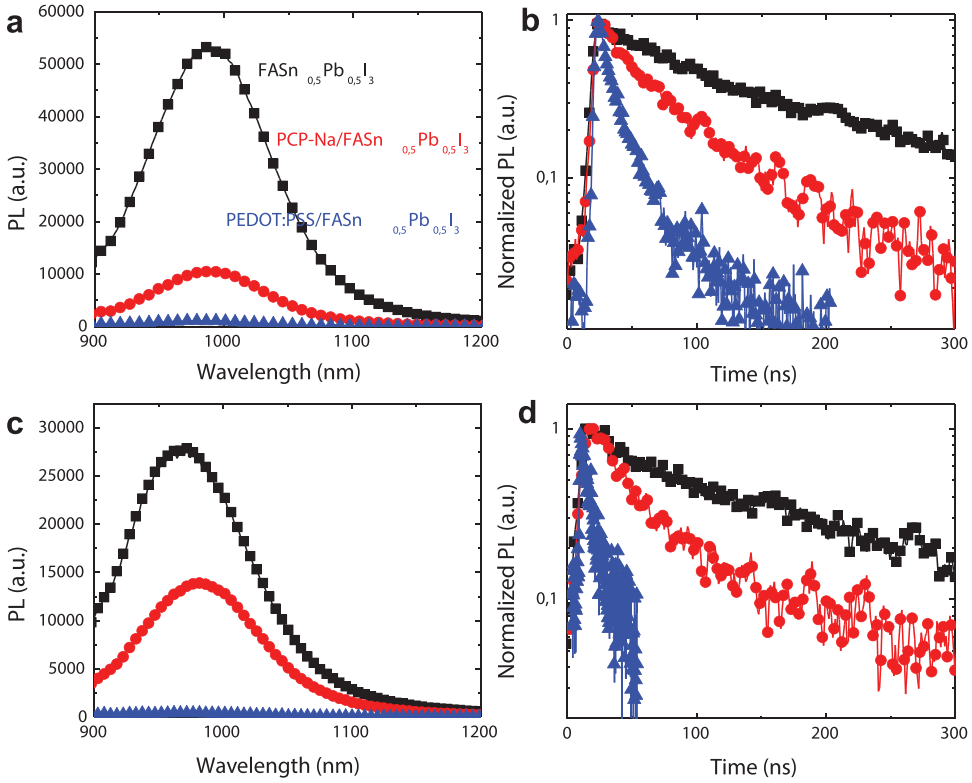

Figure 4. a,c) Steady state spectra and b,d) time resolved PL decays of $FASn_{0.5}Pb_{0.5}I_3$ films on quartz, quartz/PEDOT:PSS and quartz/PCP-Na measured with the excitation from the perovskite film side (a and b) and quartz side (c and d).

contribute to the deterioration of the J_{SC}, FF, and V_{OC}. The device with area of 0.81 cm^2 using the PCP-Na HEL has a PCE of 9.34%, which loses only 43% of the PCE compared to the 0.04 cm^2 device. The drop in the PCE is mainly due to the decrease in FF, which is limited by the higher series resistance (14 Ω cm^2). It is noted that the series resistance of the large area device using PCP-Na is much lower than the one of the PEDOT:PSS based device, probably benefiting from the higher conductivity of PCP-Na and/or due to the pin-hole free $FASn_{0.5}Pb_{0.5}I_3$ film, which also contributes to the relatively constant J_{SC} and V_{OC}.

It is also important to note that also a more standard perovskite active layer such as $FAPbI_3$ when grown on PCP-Na displays substantially higher performance in the device than the one fabricated on PEDOT:PSS.[31]

We further performed steady state and time resolved photoluminescence (PL) measurements for pristine $FASn_{0.5}Pb_{0.5}I_3$ film/quartz substrate, $FASn_{0.5}Pb_{0.5}I_3$ film/PEDOT:PSS/quartz substrate, and $FASn_{0.5}Pb_{0.5}I_3$ film/PCP-Na/quartz substrate samples. The photoluminescence of all samples was measured in transmission configuration exciting with a 400 nm pulsed laser from the $FASn_{0.5}Pb_{0.5}I_3$ layer side, as well as from the quartz side. Regardless of the side from which the sample is excited, the pure $FASn_{0.5}Pb_{0.5}I_3$ film shows the highest PL intensity with the peak emission centered around 990 nm (1.25 eV), due to the absence of charge transfer (see **Figure 4**a,c). The $FASn_{0.5}Pb_{0.5}I_3$ films coated on top of PEDOT:PSS and PCP-Na HELs show significant PL quenching due to combined effects of the hole transfer from the perovskite to HELs or the trap-assisted non-radiative recombination. Note that the $FASn_{0.5}Pb_{0.5}I_3$ film on top of PCP-Na has much stronger PL intensity compared to that on top of PEDOT:PSS, indicating much stronger radiative recombination from the band-to-band recombination of the free holes and electrons. As discussed earlier, PCP-Na HEL improves the hole injection at the anode interface due to the favorable energy level alignment. Under this circumstance, the high PL intensity is most probably due to the lower trap density of the $FASn_{0.5}Pb_{0.5}I_3$ film on top of PCP-Na, which is in line with the previous observation of a better film morphology of $FASn_{0.5}Pb_{0.5}I_3$ film on PCP-Na substrate. The elimination of the "open" grain boundaries and "hollow" grains effectively lowers the trap density in the $FASn_{0.5}Pb_{0.5}SnI_3$ film, suppressing the trap assisted non-radiative recombination and improving the V_{OC}. The PL decay dynamics of the samples follow the same trend as the steady state PL results and indicate that the charge carriers survive much longer in the $FASn_{0.5}Pb_{0.5}I_3$ film on top of PCP-Na due to the reduced trapping rate.

At this point we studied the light intensity dependence of the V_{oc} to seek other evidence about the trap assisted recombination in the devices with the two HELs. Figure S8 of the Supporting Information shows the semilogarithmic plots of the V_{OC} versus light intensity of the two types of devices. The device using PCP-Na exhibits a much smaller slope (1.05 kT q^{-1}) compared to the device using PEDOT:PSS HEL (1.80 kT q^{-1}), confirming the suppressed trap-assisted recombination losses in the device using PCP-Na HEL.[7]

Impedance spectroscopy has been intensively used to understand and distinguish electronic and ionic processes occurring

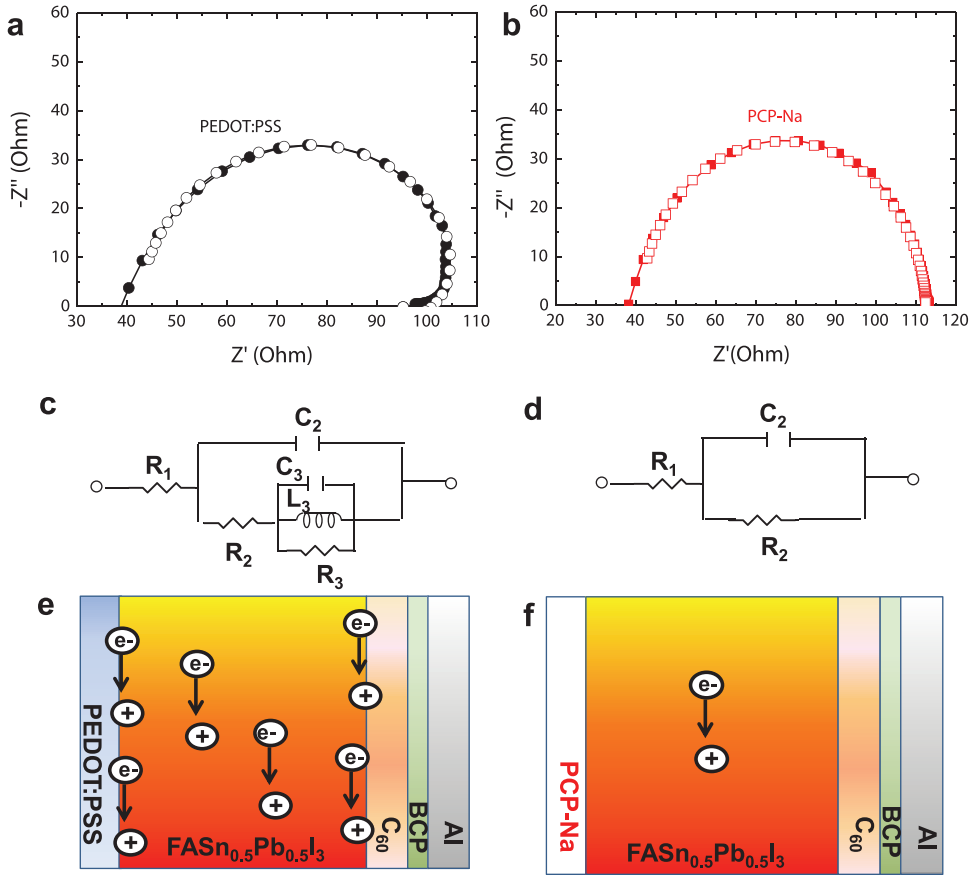

Figure 5. Impedance spectra tested at open-circuit condition under 1 sun illumination and the corresponding equivalent circuits of the devices using a,c) PEDOT:PSS and b,d) PCP-Na as HEL. (Note: The closed/open symbol represents experimental/fitting data.) Schematic illustration of the charge recombination process indicated by the black arrow in the device in case of e) PEDOT:PSS and f) PCP-Na HEL.

in the bulk of the perovskite film and at the interfacial contacts in operating HPSCs.[32–34] **Figure 5** shows the complex impedance plots (Z', $-Z''$) recorded at open-circuit voltage under 1 sun illumination for the HPSCs using PCP-Na and PEDOT:PSS HELs. Since no current flows through the device at open-circuit condition, all the photogenerated free charge carriers must recombine. The impedance plot of the device using PEDOT:PSS shows deformed semicircle at high frequency (>10 kHz) and an inductive loop at the intermediate frequency (<10 KHz), which can be fitted with an equivalent circuit as shown in Figure 5c, consisting of the contributions from the series resistance (R_1), the recombination of the charge carriers in the bulk of the perovskite film (capacitance C_2 and recombination resistance R_2), and the interfacial charge recombination at the perovskite/charge extraction layer (capacitance C_3, inductance L_3 and R_3 assigned to the inductive loop).[27–29] The charge carrier lifetime in this device is 0.86 µs ($\tau = R_2C_2$). The deformed semicircle at high frequency indicates inhomogeneity probably due to nonuniform $FASn_{0.5}Pb_{0.5}I_3$ film morphology, where severe trap-assisted recombination occurs at the pin-holes (Figure 5e). While the presence of the inductive loop indicates severe interfacial recombination at the perovskite/PEDOT:PSS or perovskite/C60 interface due to the surface trap states (Figure 5e). The impedance plot of the device using PCP-Na as HEL shows one semicircle without obvious deformation, which can be fitted well by the equivalent circuit consisting of R_1, C_2, and R_2 components as shown in Figure 5d. Compared to the device using PEDOT:PSS, the charge carrier in the device using PCP-Na has a much longer lifetime of 1.47 µs. This indicates that the bulk recombination rate of charge carriers in the perovskite film is significantly reduced in this case. Moreover, the absence of the inductive loop at intermediate frequency indicates the absence of charge recombination at the perovskite/PCP-Na (C60) interfaces (Figure 5f). Therefore, the reduced interfacial and bulk charge recombination contributes to the enhancement of the performance in the device using PCP-Na as HEL.

In conclusion, we demonstrated that the hole extraction layer significantly influences the interfacial recombination and bulk recombination of the charge carriers and therefore the performance of the $FASn_{0.5}Pb_{0.5}I_3$ based HPSCs. $FASn_{0.5}Pb_{0.5}I_3$ film grown on PEDOT:PSS display large pin-holes both at the grain boundaries and in the grains, leading to significant bulk and interfacial charge recombination. The same perovskite layer grown on PCP-Na is compact and pin-hole free. The high quality of the $FASn_{0.5}Pb_{0.5}I_3$ film has the effect of reducing effectively the shunts and the trap states. Moreover, PCP-Na favorably aligns the HOMO level with the valence band of the perovskite layer, improving in this way the charge extraction. Consequently, the interfacial and bulk recombination of the

charge carriers in the device fabricated on PCP-Na is effectively reduced compared to devices fabricated on PEDOT:PSS, leading to a 40% improvement in the PCE. PCP-Na is a better candidate for large area devices compared to PEDOT:PSS.

Experimental Section

Materials: PEDOT:PSS water dispersion (Clevios VP AI 4083) was acquired from Heraeus. FAI (>98%) and PbI_2 (>99.99%) were purchased from TCI EUROPE N.V. SnI_2 (99.99%), SnF_2 (>99%), C60 (>99.9%), BCP (99.99%), DMF (99.8%), and DMSO (99.8%) were purchased from Sigma-Aldrich. All the materials were used as received without further purification. PCP-Na was synthesized following procedure reported in literature.[26]

Device Fabrication and Characterization: ITO glasses were cleaned using an ultrasonication bath in soap water and rinsed sequentially with deionized water, acetone, and isopropyl alcohol. A PEDOT:PSS layer was then spin-coated onto the ITO substrates at 3000 rpm for 60 s. PCP-Na layers with 1.5–10 nm were spin-coated at 3000 rpm for 30 s on top of the ITO substrate from mixed solvents of water and methanol with a volume ratio of 3:7. The coated substrates were dried at 140 °C for 20 min and then transferred to a nitrogen-filled glove-box. The $FASn_{0.5}Pb_{0.5}I_3$ film was spin-coated from a precursor solution comprising 1 M FAI, 0.5 M SnI_2, 0.5 M PbI_2, and 0.05 M SnF_2 in mixed solvents of DMSO and DMF (1:4 volume ratio) at 4000 rpm for 60 s. Diethyl ether was used as the antisolvent during the spin-coating process. $FASn_{0.5}Pb_{0.5}I_3$ films were annealed at 100 °C for 10 min. Next, 60 nm C60, 6 nm BCP, and 100 nm Al layers were sequentially evaporated on top of the perovskite film under vacuum of $<10^{-6}$ mbar. The *J–V* curves of the HPSCs were measured at 295 K using a Keithley 2400 source meter under simulated AM 1.5 G solar illumination using a Steuernagel Solar constant 1200 metal halide lamp in a nitrogen-filled glove box. The light intensity was calibrated to be 100 mW cm^{-2} by using a Si reference cell and correcting the spectral mismatch. A shadow mask (0.04 cm^2) was used to exclude lateral contributions beyond the device area.

PL Measurement: The samples were measured in an inert atmosphere and excited at 400 nm by the second harmonic of a mode-locked Ti:sapphire (Mira 900) laser delivering pulses of 150 fs. The repetition rate of the laser is 76 MHz; a pulse picker was inserted in the optical path to decrease the repetition rate of the laser pulses. The excitation beam was focused with a 150 mm focal length lens, and the emission was collected and coupled into a spectrometer with a 50 lines mm^{-1} grating. The steady-state PL was recorded with an Image EM CCD camera from Hamamatsu (Hamamatsu, Japan). Time-resolved PL was measured with a Hamamatsu streak camera working in single sweep mode.

GIWAXS Measurement: The measurement was performed using at the MINA instrument at the University of Groningen, with an X-ray scattering instrument built on a Cu rotating anode source ($\lambda = 1.5413$ Å). 2D patterns were collected using a Vantec500 detector (1024 × 1024 pixel array with pixel size 136 × 136 µm) located 93 mm away from the sample. The thin films were placed in reflection geometry at certain incident angles α_i with respect to the direct beam using a Huber goniometer. GIWAXS patterns were acquired using incident angles of 0.2° (close to the incident angle of the materials). An exposure time of 1 h per pattern was used. The direct beam center position on the detector and the sample-to-detector distance were calibrated using the diffraction rings from standard silver behenate and Al_2O_3 powders. All the necessary corrections for the GIWAXS geometry were applied to the raw patterns using the GIXGUI Matlab toolbox.

Other Thin Film Characterization: AFM topographical images were recorded in ScanAsyst Mode on a Bruker Multimode 8 microscope with ScanAsyst Air probes (resonant frequency 70 kHz, spring constant 0.4 N m^{-1}) at a scan rate of 0.8 Hz and a resolution of 800 samples per line. The data were later analyzed with Nanoscope Analysis 1.5 (Bruker). SEM images were recorded in air on an FEI NovaNano SEM 650 with an acceleration voltage of 5 kV. UV–vis spectra of the perovskite films were recorded on Shimatzu UV–vis–NIR spectrophotometer (UV 3600).

Impedance Measurement: The *C–V* measurements were conducted under dark condition at a frequency of 10 kHz with an ac drive voltage of 20 mV and DC bias in the range of –1.0 to 1.0 V on a Solarton 1260 impedance gain-phase analyzer. The *C–f* measurements were conducted with a SP-200 Bio-Logic potentiostat equipped with an electrochemical impedance spectroscopy analyzer by applying a 25 mV ac signal at open-circuit voltage under 1 sun illumination.

Supporting Information

Supporting Information is available from the Wiley Online Library or from the author.

Acknowledgements

The authors thank Dr. Graeme Blake for the discussion about the XRD and SEM results, and Dr. Jian Liu for the film thickness measurement by ellipsometry. The authors also thank Arjen Kamp and Teo Zaharia for their kind technical support in the laboratory.

Conflict of Interest

The authors declare no conflict of interest.

Keywords

charge recombination, half tin and lead perovskite, hole extraction layer, solar cells, trap states

Received: June 11, 2018
Published online: July 10, 2018

[1] M. M. Lee, J. Teuscher, T. Miyasaka, T. N. Murakami, H. J. Snaith, *Science* **2012**, *338*, 643.
[2] J. Burschka, N. Pellet, S.-J. Moon, R. Humphry-Baker, P. Gao, M. K. Nazeeruddin, M. Grätzel, *Nature* **2013**, *499*, 316.
[3] J.-H. Im, C.-R. Lee, J.-W. Lee, S.-W. Park, N.-G. Park, *Nanoscale* **2011**, *3*, 4088.
[4] A. Kojima, K. Teshima, Y. Shirai, T. Miyasaka, *J. Am. Chem. Soc.* **2009**, *131*, 6050.
[5] S. Shao, M. Abdu-Aguye, L. Qiu, L.-H. Lai, J. Liu, S. Adjokatse, F. Jahani, M. E. Kamminga, G. H. ten Brink, T. T. M. Palstra, B. J. Kooi, J. C. Hummelen, M. Antonietta Loi, *Energy Environ. Sci.* **2016**, *9*, 2444.
[6] A. Dubey, N. Adhikari, S. Venkatesan, S. Gu, D. Khatiwada, Q. Wang, L. Mohammad, M. Kumar, Q. Qiao, *Sol. Energy Mater. Sol. Cells* **2016**, *145*, 193.
[7] S. Shao, M. Abdu-Aguye, T. S. Sherkar, H.-H. Fang, S. Adjokatse, G. H. ten Brink, B. J. Kooi, L. J. A. Koster, M. A. Loi, *Adv. Funct. Mater.* **2016**, *26*, 8094.
[8] N. J. Jeon, J. H. Noh, Y. C. Kim, W. S. Yang, S. Ryu, S. Il Seok, *Nat. Mater.* **2014**, *13*, 897.
[9] S. Shao, J. Liu, H.-H. Fang, L. Qiu, G. H. ten Brink, J. C. Hummelen, L. J. A. Koster, M. A. Loi, *Adv. Energy Mater.* **2017**, *7*, 1701305.

[10] M. Saliba, T. Matsui, J.-Y. Seo, K. Domanski, J.-P. Correa-Baena, M. K. Nazeeruddin, S. M. Zakeeruddin, W. Tress, A. Abate, A. Hagfeldt, M. Gratzel, *Energy Environ. Sci.* **2016**, *9*, 1989.
[11] H.-S. Kim, C.-R. Lee, J.-H. Im, K.-B. Lee, T. Moehl, A. Marchioro, S.-J. Moon, R. Humphry-Baker, J.-H. Yum, J. E. Moser, M. Grätzel, N.-G. Park, *Sci. Rep.* **2012**, *2*, 591.
[12] J. Liu, S. Lu, L. Zhu, X. Li, W. C. H. Choy, *Nanoscale* **2016**, *8*, 3638.
[13] H. Yu, H. Lu, F. Xie, S. Zhou, N. Zhao, *Adv. Funct. Mater.* **2016**, *26*, 1411.
[14] J. Qing, X.-K. Liu, M. Li, F. Liu, Z. Yuan, E. Tiukalova, Z. Yan, M. Duchamp, S. Chen, Y. Wang, S. Bai, J.-M. Liu, H. J. Snaith, C.-S. Lee, T. C. Sum, F. Gao, *Adv. Energy Mater.* **2018**, https://doi.org/10.1002/aenm.201800185.
[15] L. Weiqiang, Z. Dewei, Y. Yue, G. C. R., W. Changlei, C. A. J., S. Philip, M. Weiwei, Z. Kai, X. Ren-Gen, Y. Yanfa, *Adv. Mater.* **2016**, *28*, 9333.
[16] N. K. Noel, S. D. Stranks, A. Abate, C. Wehrenfennig, S. Guarnera, A.-A. Haghighirad, A. Sadhanala, G. E. Eperon, S. K. Pathak, M. B. Johnston, A. Petrozza, L. M. Herz, H. J. Snaith, *Energy Environ. Sci.* **2014**, *7*, 3061.
[17] S. Shao, J Liu, G. Portale, H.-H. Fang, G. Blake, H. H. ten Brink, L. A. Koster, M. A. Loi, *Adv. Energy Mater.* **2017**, *8*, 1702019.
[18] Y. Ogomi, A. Morita, S. Tsukamoto, T. Saitho, N. Fujikawa, Q. Shen, T. Toyoda, K. Yoshino, S. S. Pandey, T. Ma, S. Hayase, *J. Phys. Chem. Lett.* **2014**, *5*, 1004.
[19] F. Hao, C. C. Stoumpos, R. P. H. Chang, M. G. Kanatzidis, *J. Am. Chem. Soc.* **2014**, *136*, 8094.
[20] W. Shockley, H. J. Queisser, *J. Appl. Phys.* **1961**, *32*, 510.
[21] F. Zuo, S. T. Williams, P.-W. Liang, C.-C. Chueh, C.-Y. Liao, A. K.-Y. Jen, *Adv. Mater.* **2014**, *26*, 6454.
[22] Z. Yang, R. Adharsh, C.-C. Chueh, J. S. Byeok, L. Bo, Z. Ting, A. K.-Y. Jen, *Adv. Mater.* **2016**, *28*, 8990.
[23] M. Lyu, M. Zhang, N. A. Cooling, Y. Jiao, Q. Wang, J.-H. Yun, B. Vaughan, G. Triani, P. Evans, X. Zhou, K. Feron, A. Du, P. Dastoor, L. Wang, *Sci. Bull.* **2016**, *61*, 1558.
[24] G. E. Eperon, T. Leijtens, K. A. Bush, R. Prasanna, T. Green, J. T.-W. Wang, D. P. McMeekin, G. Volonakis, R. L. Milot, R. May, A. Palmstrom, D. J. Slotcavage, R. A. Belisle, J. B. Patel, E. S. Parrott, R. J. Sutton, W. Ma, F. Moghadam, B. Conings, A. Babayigit, H.-G. Boyen, S. Bent, F. Giustino, L. M. Herz, M. B. Johnston, M. D. McGehee, H. J. Snaith, *Science* **2016**, *354*, 861.
[25] D. Zhao, Y. Yu, C. Wang, W. Liao, N. Shrestha, C. R. Grice, A. J. Cimaroli, L. Guan, R. J. Ellingson, K. Zhu, X. Zhao, R.-G. Xiong, Y. Yan, *Nat. Energy* **2017**, *2*, 17018.
[26] Y. Cui, B. Xu, B. Yang, H. Yao, S. Li, J. Hou, *Macromolecules* **2016**, *49*, 8126.
[27] S. Shao, Z. Chen, H.-H. Fang, G. H. ten Brink, D. Bartesaghi, S. Adjokatse, L. J. A. Koster, B. J. Kooi, A. Facchetti, M. A. Loi, *J. Mater. Chem. A* **2016**, *4*, 2419.
[28] C. Zuo, L. Ding, *Adv. Energy Mater.* **2017**, *7*, 1601193.
[29] C. Zuo, D. Vak, D. Angmo, L. Ming, M. Gao, *Nano Energy* **2018**, *46*, 185.
[30] C. Zuo, H. J. Bolink, H. Han, J. Huang, D. Cahen, L. Ding, *Adv. Sci.* **2016**, *3*, 1500324.
[31] S. Shao, Y. Cui, H. Dium, J. Hou, M. A. Loi, unpublished.
[32] A. Guerrero, G. Garcia-Belmonte, I. Mora-Sero, J. Bisquert, Y. S. Kang, T. J. Jacobsson, J.-P. Correa-Baena, A. Hagfeldt, *J. Phys. Chem. C* **2016**, *120*, 8023.
[33] J.-P. Correa-Baena, S.-H. Turren-Cruz, W. Tress, A. Hagfeldt, C. Aranda, L. Shooshtari, J. Bisquert, A. Guerrero, *ACS Energy Lett.* **2017**, *2*, 681.
[34] F. Fabregat-Santiago, M. Kulbak, A. Zohar, M. Vallés-Pelarda, G. Hodes, D. Cahen, I. Mora-Seró, *ACS Energy Lett.* **2017**, *2*, 2007.